applied sciences

MDPI

Article

Optimal Design of a Six-Phase Permanent-Magnet-Assisted Synchronous Reluctance Motor to Convert into Three Phases for Fault-Tolerant Improvement in a Traction System

Daeil Hyun, Donghan Yun and Jeihoon Baek *

Electrical & Electronics and Communication Engineering Department, Koreatech University, Cheonan-si 31253, Korea; hdi0530@koreatech.ac.kr (D.H.); dk03149@koreatech.ac.kr (D.Y.)
* Correspondence: jhbaek@koreatech.ac.kr; Tel.: +82-41-560-1258

Abstract: A six-phase motor with a high degree of freedom can be converted into a three-phase motor in order to be used in a traction system. In addition, when phase-change technology is applied, it is possible to establish an efficient control strategy tailored to the driving environment of the EVs. Therefore, in this paper, a down-scaled 3 kW permanent-magnet-assisted synchronous motor (PMa-SynRM) capable of phase switching was designed, and its driving states in controlled fault modes were analyzed through experiments. The PMa-SynRM selected for this study was a machine that had good fault-tolerance capabilities and was less expensive than an IPMSM with the same performance; it was designed using the lumped-parameter method (LPM) having a fast calculating speed and a genetic algorithm. In addition, the effectiveness of the optimal design was verified by comparing the analytical results of the FEM and the LPM. Lastly, a phase switching experiment was conducted to analyze the steady-state and transient-state characteristics, and the results are presented.

Keywords: six-phase; optimal design; fault-tolerant; lumped parameter method; phase switching; traction system; electric vehicle

Citation: Hyun, D.; Yun, D.; Baek, J. Optimal Design of a Six-Phase Permanent-Magnet-Assisted Synchronous Reluctance Motor to Convert into Three Phases for Fault-Tolerant Improvement in a Traction System. *Appl. Sci.* **2021**, *11*, 8508. https://doi.org/10.3390/app11188508

Academic Editor: Gang Lei

Received: 28 July 2021
Accepted: 7 September 2021
Published: 13 September 2021

1. Introduction

A three-phase induction machine (IM) is a structure that is simple and widely used in industry. It is tough, durable, and affordable, has the advantages of easy maintenance, and has few faults. However, efficiency can be greatly reduced due to the loss of short-circuit current flowing internally within the rotor, and there is the disadvantage of a low-torque characteristic in the low-speed region [1]. These disadvantages have been improved through research on multiphase IMs with higher output power and reliability as power electronics technology developed [2–6], and the use of IMs in electric-vehicle (EV) traction applications such as trains, ships, and automobiles was expanded [7–9].

While IMs with robustness and low manufacturing costs are widely used in various industrial fields, their relatively low efficiency and low torque characteristics at low speeds are indicated as disadvantages in traction systems [10–12]. Therefore, a permanent-magnet synchronous machine (PMSM) that can overcome these drawbacks and satisfy conditions such as high torque at low speed, wide rated output power range, reliability, robustness, and reasonable cost, was proposed as an alternative [1,10]. In addition, a PMSM applied to a hybrid electric vehicle (HEV) has a higher power density-to-volume ratio than an IM, so it is valuable as an alternative electric motor to the IM in terms of the environment and fuel consumption [11].

However, the rare earth element permanent magnet used in a PMSM is treated as a national strategic resource and has the risk of cost increments due to an imbalance in the supply and demand of materials, and therefore the manufacturing cost may significantly increase depending on the used amount [12]. Therefore, a permanent-magnet-assisted synchronous-reluctance machine (PMa-SynRM) was proposed as an alternative to reduce

this risk [13]. A PMa-SynRM, which can show similar performance to that of an interior permanent-magnet synchronous machine (IPMSM), is a type of motor that reduces the use of magnets in an IPMSM and increases the proportion of reluctance torque through the design of the magnetic flux barrier of the rotor. When the amount of permanent magnet (PM) material is large, there is a risk of PM demagnetization during field weakening control to suppress back electromotive force due to high-speed rotation, and excessive current may be induced from high flux linkage during a short-circuit phase [14–16].

In traction systems, reliability, safety, and high power density must be ensured [1,16]. If operation cannot continue due to a fault in the inverter or the motor that occurs on the train, secondary accidents will be increasingly possible in cars that use an existing three-phase traction system. Some typical types of faults are cases in which current does not flow to a phase due to an open winding of the motor, or in which excessive current flows through a faulty short-circuit phase.

To overcome the unreliability and safety problems of such a three-phase traction system, the authors of [16] proposed a triple-redundant nine-phase PMa-SynRM with improved fault-tolerance and suggested solutions for two fault scenarios. A faulty current due to short-circuit was analyzed as the worst-case fault scenario. However, although the proposed motor was a nine-phase system composed of three windings, it was essentially a three-phase system and had no additional advantages other than the merits of continuous operation in case of a fault.

Therefore, a multi-phase machine was proposed as an alternative to operating continuously during a failure that occurs in the motor or inverter, which would also improve output power density [2–7,17–29]. Fault-tolerance research due to the high flexibility of multi-phase electric motors led to an ongoing study from 1990 until recently [16–31]. In particular, research results on the design and control of five-phase motors have consistently been published in academia [17–22], and studies related to six-phase motors are also steadily progressing, yielding good results [23–31].

In particular, a six-phase motor has twice the number of degrees of freedom of current control compared to a three-phase motor, so it has excellent fault-tolerance capabilities, and can be applied to improve output power density [23,30,31]. For example, the authors of [30] analyzed through simulation that continuous operation was possible even when three out of six phases were lost due to a fault. If a fault occurs in one phase of the motor, the state is as shown in Figure 1. The authors of [31] showed the results of a study on the improvement of power density through fifth and seventh harmonic injection using the space-vector pulse-width modulation (SVPWM) control method in a six-phase PMSM. In addition, from a design point of view, the winding coefficient of a six-phase motor with the same pole slot combination is equal to or higher than that of a three-phase motor, which is advantageous in terms of efficiency, power density, and costs [24]. It is also advantageous for balancing the spatial harmonics of the magnetomotive force that causes torque pulsation, and it is easy to obtain stable torque-output and speed-control characteristics [27].

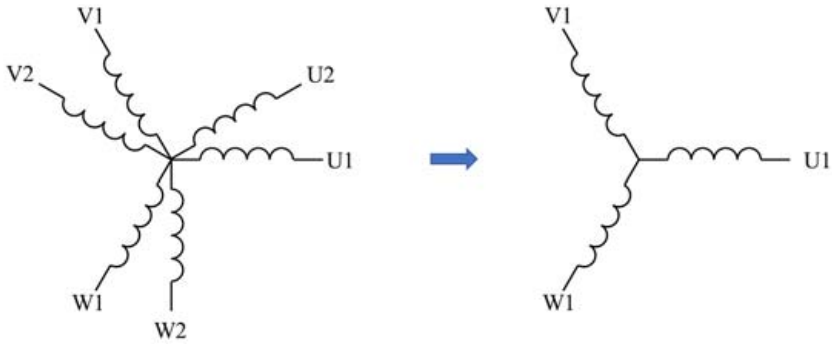

Figure 1. Phase switching from six to three phases.

The optimal design of an IPMSM or PMa-SynRM was determined by analyzing the magnetic equivalent circuit (MEC) using the lumped-parameter method (LPM), which is characterized by fast analysis and finding optimal candidate models through the genetic algorithm [21]. The optimal design of this method was established for a five-phase motor with a two-layer structure, but has not been previously attempted for an asymmetric six-phase PMa-SynRM. In addition, since the fault-tolerance capability of the six-phase motor presented in [30] was not experimentally verified, it was necessary to evaluate its feasibility. Therefore, this paper investigated the optimal design of a 3 kW six-phase down-scaled model of a PMa-SynRM type, which could respond flexibly to fault situations, had excellent traction, and reduced PM usage; it was conducted using LPM and the genetic algorithm, and fault-tolerant capability was confirmed by analyzing the load characteristics for six- and three-phase operations.

This paper is organized as follows. Section 2 describes the optimal design process of PMa-SynRM with asymmetric winding of a six-phase two-layer rotor structure. Section 3 analyzes the LPM and FEM results at the test point of the optimally designed motor, and Section 4 compares and analyzes the steady-state load test results of the PMa-SynRM. Section 5 analyzes the transient-state during switching from six to three phases.

2. Design Process Using Lumped-Parameter Method (LPM)

The ideal traction motor, which has high power density and efficiency, constant power speed range, robustness, reliability, and low cost, must be able to operate as a general-purpose inverter. However, it is difficult to design a motor that can satisfy all of these conditions. Nevertheless, we can design optimized motors through various methods due to developments in the understanding of design technology for motors, and analysis in order to produce designs close to the desired performance level can be carried out using LPM. Although LPM has the disadvantage of lower accuracy than that of FEM, it is characterized by fast analysis, and therefore can produce results in the desired direction by the designer in a short amount of time, making it a powerful tool for the design of initial prototype motors. The main parameters to be analyzed in LPM are the magnetic flux, inductance of the phase currents, and stator and rotor shapes. To increase output power density, which is the main goal of the motor, a large torque must be generated with a small current, and the total weight must be light. Therefore, if the magnetic flux, current, and inductance are designed properly in the torque, as shown in Equation (1), output torque can be improved.

$$T_{em} = T_m + T_r = \frac{m}{2} p\left[\lambda_{pm} i_d + \left(L_q - L_d\right) i_d i_q\right] \quad (1)$$

2.1. Q-Axis PM Flux Linkage

In LPM, performance is analyzed through the magnetic flux generated by the shape of the stators and rotors on the basis of the magnetic circuit. Figure 2 shows the magnetic circuit of the PMa-SynRM, which can be regarded as a linear MEC consisting of three magnetic flux sources and four magnetic resistances in a rotor shape with a two-layered magnetic flux barrier. The first magnetic flux source was generated from the permanent magnet, and the total magnetic flux could be calculated by determining the residual magnetic flux density of the permanent magnet from the area in which the permanent magnet and the iron core come into contact. The second magnetic flux source was located on a bridge at the end of the second-layer magnetic flux barrier that connected the inner core of the rotor and the outer core in front of the permanent magnets. The third magnetic flux source was located at the bridge at the end of the first-layer flux barrier with opposite polarity. The magnitude of the magnetic flux source was calculated as the product of the saturation magnetic flux density of the iron core and the bridge area, and the formula is shown in Equation (2). In addition, the magnetic resistance due to the gap between the stator and the rotor was determined as in Equation (3), and the magnetic resistance of the magnetic flux barrier inserted with the permanent magnet was a linear value, as shown in Equation (4).

$$\varnothing_m = B_r A_m,\ \varnothing_b = B_{sat} A_b \tag{2}$$

$$r_{g1} = \frac{g}{\mu_0 A_{g1}},\ r_{g2} = \frac{g}{\mu_0 A_{g2}} \tag{3}$$

$$r_{m1} = \frac{l_{c1}}{\mu_0 A_{c1}},\ r_{m2} = \frac{l_{c2}}{\mu_0 A_{c2}} \tag{4}$$

where $\varnothing_m$: magnetic flux by permanent magnet (Wb), B_r: residual magnetic flux density of the permanent magnet (T), A_m: contact area between the iron core and the permanent magnet (m^2), A_b: cross-sectional area of bridge (m^2), $\varnothing_b$: magnetic flux through the bridge (Wb), B_{sat}: iron core saturation magnetic flux density (T), r_{m1}, r_{m2}: magnetic resistance of PM (H^{-1}), l_{c1}, l_{c2}: thickness of magnetic flux barrier (m), A_{c1}, A_{c2}: cross-sectional area of magnetic flux barrier (m^2), A_{g1}, A_{g2}: air-gap cross-sectional area (m^2).

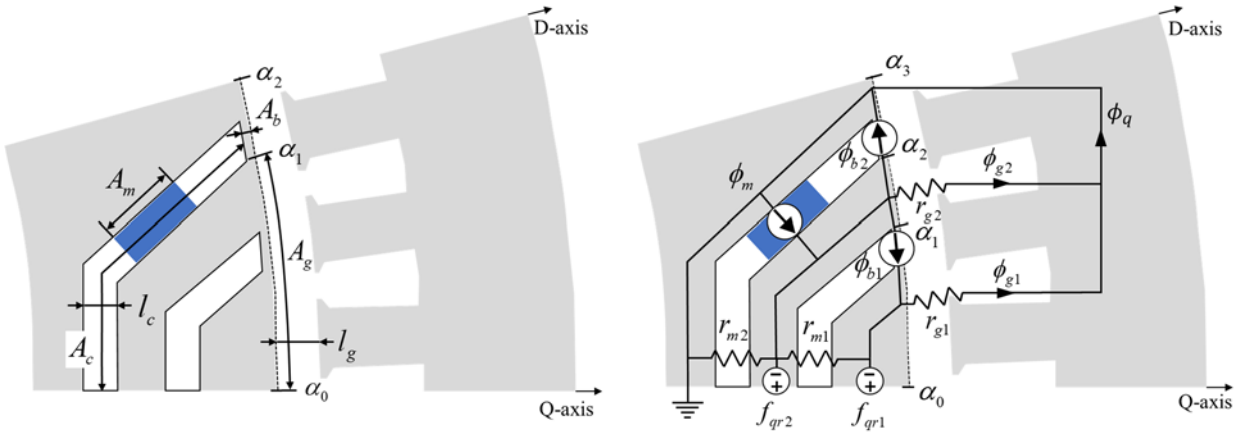

Figure 2. Magnetic equivalent circuit (MEC) for PM flux linkage. (**a**) Geometric definition for reluctances; (**b**) Q-axis linear MEC for PM flux linkage.

The air-gap magnetic flux density was calculated through Equations (5) and (6) on the basis of the principle of superposition. Using air-gap flux density for each section, the superimposed fundamental wave air-gap magnetic flux density was obtained through Equation (7) using the Fourier series. Here, the fundamental wave denotes the frequency of the air gap MMF corresponding to the number of pole pairs of the motor. Therefore, the no-load flux linkage could be obtained through Equation (8).

$$B_{g1} = \varnothing_m / A_{eq1} + \varnothing_{b1} / A_{eq2} + \varnothing_{b2} / A_{eq3} \tag{5}$$

$$B_{g2} = \varnothing_m / A_{eq4} + \varnothing_{b1} / A_{eq5} + \varnothing_{b2} / A_{eq6} \tag{6}$$

$$B_1 = \frac{4}{\pi}\left[B_{g1}(\sin(\alpha_0) - \sin\alpha_1) + B_{g2}(\sin(\alpha_1) - \sin(\alpha_2))\right] \tag{7}$$

$$\lambda_{PM} = \frac{\sqrt{2} r l B_1 N_a k_w}{p} \tag{8}$$

where B_{g1}, B_{g2}: air-gap flux density in the first and second sections (T), A_{eq1}, A_{eq2}: equivalent area affected by magnetic flux source (m^2), B_1: magnitude of fundamental wave of air-gap magnetic flux density (T), r: inner diameter of stator (m), l: lamination length (m), λ_{PM}: no-load flux linkage (Wb).

2.2. D, Q-Axis Inductance

Figure 3 shows the magnetomotive force (MMF) formed by the D, Q-axis current, and the flow of the flux. Similarly to calculating the magnetic circuit of Q-axis PM flux linkage, calculating the flux linkage for Q-axis inductance of the MEC in Figure 3a considered only linear reluctance. In general, it was assumed that Q-axis inductance was constant, because linear reluctance is dominant under the influence of the magnetic flux barrier in PMSM when having a two-layer structure or more [21]. Therefore, Q-axis inductance was calculated through the MMF caused by the Q-axis current generated in the winding of the stator and the linear MEC composed of the magnetic resistance component of the air-gap and the magnetic flux barrier.

$$F_q = \frac{m}{2}\frac{4}{\pi}\frac{N_a k_w p}{2}\sqrt{2}I_q \tag{9}$$

$$f_{qs1} = F_q\frac{\cos(\alpha_0) - \cos(\alpha_1)}{\alpha_1 - \alpha_0} \tag{10}$$

$$f_{qs2} = F_q\frac{\cos(\alpha_1) - \cos(\alpha_2)}{\alpha_2 - \alpha_1} \tag{11}$$

where F_q: magnitude of fundamental wave of MMF by the Q-axis (AT), f_{qs1}: magnitude of MMF between α_0 and α_1 (AT), f_{qs2}: magnitude of MMF between α_1 and α_2 (AT).

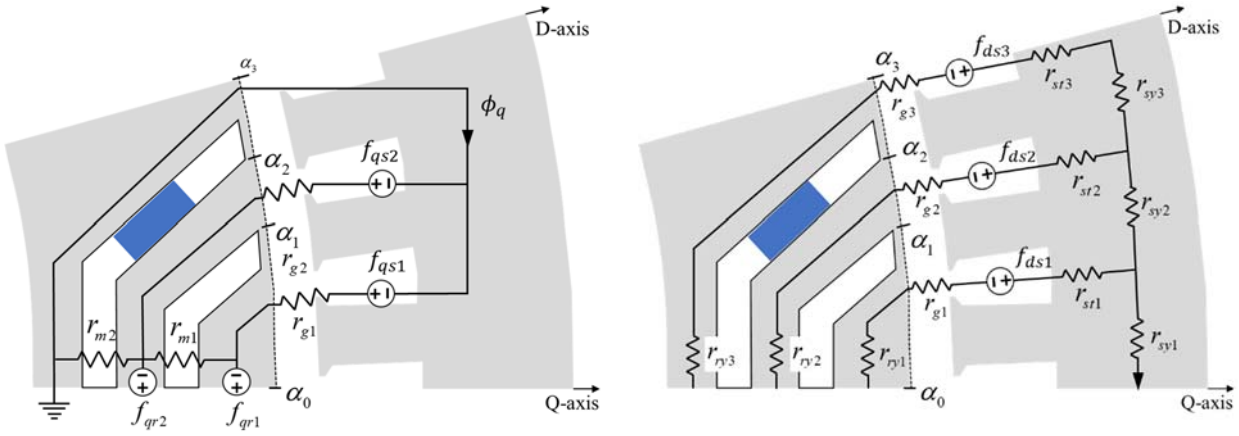

(**a**) (**b**)

Figure 3. Magnetic equivalent circuit for (**a**) Q-axis current (**b**) D-axis current.

Since MEC analysis aims to obtain the magnetic flux and inductance flowing in the air gap, it could be formulated as Equation (12) by applying the principle of superposition. Therefore, air-gap magnetic flux density was obtained by dividing the magnetic flux for each section by the air-gap area, and the magnitude of the fundamental component of the air-gap magnetic flux density was calculated through Equations (13) and (14). Lastly, the Q-axis inductance was obtained through the calculated air-gap flux density from Equation (15).

$$\varnothing_{qg1} = \frac{f_{qs1}R_{eq1} + f_{qs2}R_{eq2}}{r_{g1}},\ \varnothing_{qg2} = \frac{f_{qs1}R_{eq3} + f_{qs2}R_{eq4}}{r_{g2}} \tag{12}$$

$$B_{qg1} = \varnothing_{qg1}/A_{g1},\ B_{qg2} = \varnothing_{qg2}/A_{g2}, \tag{13}$$

$$B_{q1} = B_{qg1}(\alpha_1 - \alpha_0) + B_{qg2}(\alpha_2 - \alpha_1) \tag{14}$$

$$\lambda_q = \frac{2lrB_{q1}N_a k_w}{p},\ L_q = \frac{\lambda_q}{I_q} \tag{15}$$

where $\varnothing_{qg1}$, $\varnothing_{qg2}$: magnetic flux flowing through air-gap in each section (Wb), B_{qg1}, B_{qg1}: air-gap magnetic flux density in each section (T), B_{q1}: magnitude of the fundamental air-gap magnetic flux density (T), λ_q: flux linkage through D-axis current (Wb), L_q: Q-axis inductance (H).

In addition to Q-axis inductance, D-axis inductance is a major variable that determines reluctance torque, which is the second term in Equation (1). To improve efficiency, the difference between the two inductances should be maximized. Figure 3b shows the MEC for D-axis inductance, which was similar to the process of calculating the Q-axis inductance, but had to be calculated considering the saturation of iron-core characteristics. The D-axis flux flowed along the iron flux-path of the rotor by MMF generated by the D-axis current, as shown in Figure 3b. As a result, the magnitude of magnetic resistance was greatly variable due to the nonlinear saturation characteristic of the flux-path of the iron-core with high permeability, according to the magnitude of the current, and the range of variability in the D-axis inductance was also large. In the D-axis MEC, the MMF source was located in three branches, and nonlinear magnetic resistance was present in the teeth of the stator, the back iron, and two yokes of the rotor; air-gap magnetic resistance was located in each branch.

The magnitude of the fundamental component of the D-axis MMF was calculated using Equation (16), and the magnitude of MMF corresponding to each section was calculated using Equation (17). However, since magnetic resistance varies due to the nonlinear characteristics of the iron core, in order to obtain the magnetic flux flowing through each section, the magnetic flux density for each section had to be obtained using Equation (18). Equation (18) shows the MMF function of magnetic flux density and magnetic field intensity with Kirchhoff's second law applied, each term referring to the drop in MMF generated by each magnetic resistance.

$$F_d = \frac{m}{2}\frac{4}{\pi}\frac{N_a k_w p}{2}\sqrt{2}I_d \tag{16}$$

$$f_{dsn} = F_d\frac{\cos(\alpha_{n-1}) - \cos(\alpha_n)}{\alpha_1 - \alpha_0} \tag{17}$$

$$f_{dsn} = H\left(B_{ryn}\right)l_{ryn} + H(B_{stn})l_{stn} + H\left(B_{syn}\right)l_{syn} + B_{dgn}l_g/\mu_0 \tag{18}$$

where F_d: fundamental MMF through D-axis current (AT), f_{dsn}: magnitude of MMF between α_{n-1} and α_n) (AT), B_{ryn}: magnetic flux density of rotor yoke (T), B_{stn}: magnetic flux density of stator teeth (T), B_{syn}: magnetic flux density of stator yoke (T).

By applying the fsolve function, which is a nonlinear solver of MATLAB, to the BH curve of the iron-core material, the air-gap flux density vectors [B_{dg1}, B_{dg2}, B_{dg3}] were obtained as shown in the flowchart in Figure 4. Lastly, the D-axis inductance was calculated through Equations (19) and (20).

$$B_{d1} = B_{dg1}(\alpha_1 - \alpha_0) + B_{dg2}(\alpha_2 - \alpha_1) + B_{dg3}(\alpha_3 - \alpha_2) \tag{19}$$

$$\lambda_d = \frac{2lrB_{d1}N_a k_w}{p},\ L_d = \frac{\lambda_d}{I_d} \tag{20}$$

where B_{d1}: magnitude of the fundamental component of the air-gap magnetic flux density through D-axis current (T), λ_d: flux linkage through D-axis current (Wb), L_d: D-axis inductance (H).

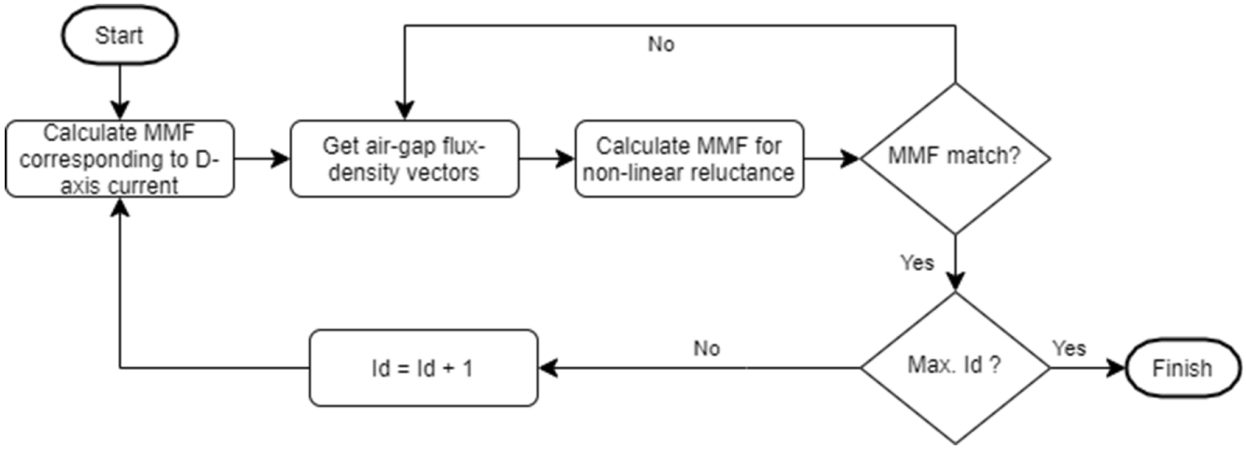

Figure 4. Calculation process for D-axis inductance in the case of a nonlinear MEC.

2.3. Optimizing the Design Process by a Genetic Algorithm and Requirement for Machine Design

The performance of the motor was calculated through magnetic-circuit analysis of the LPM, while the optimized candidate model could be obtained through the optimization model selection process in Figure 5. First, an initial design shape variable and its allowable range were set, and values within the set range were randomly selected to generate first-generation candidate models. Second, the probability of realizing the shape of the generated candidate model was determined, and motor performance was calculated through the magnetic-circuit analysis of the LPM on the basis of design variables; third, the objective function value of Equation (21) was calculated. As a result of the first-generation model having the minimal objective function value calculated, the next-generation models were created by recombining the design variable values, and the above process was repeated to derive an optimized candidate model. To evaluate the fault-tolerance of the machine, the terms of power factor and torque ripple were not included in the objective function Equation (21).

$$O.F = \sqrt{k_1(1/Efficiency)^2 + k_2(Material\ cost/Initial\ cost)^2},\ k_1 + k_2 = 1 \quad (21)$$

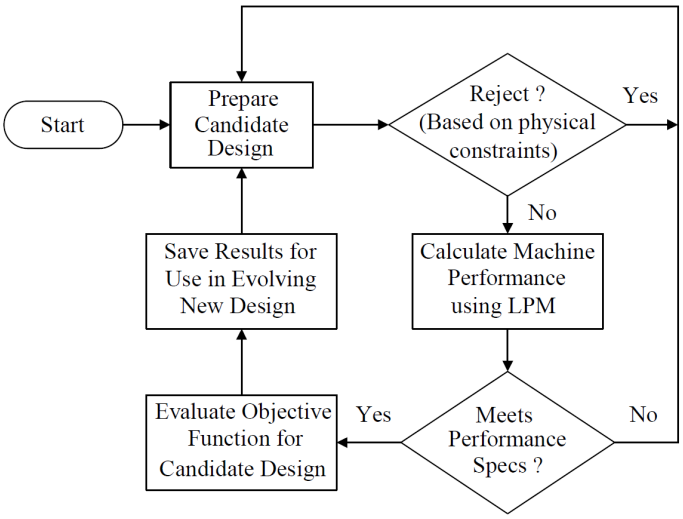

Figure 5. Flowchart describing the optimization process using LPM.

Equation (21) is composed of efficiency and cost terms, and k_1 and k_2 were set to 0.6 and 0.4 as weights for each term, respectively. These weights were calculated as ideal for deriving the optimized shape in which the objective function value was the minimum with respect to the calculated efficiency, with the cost value of the initial model as the

denominator in the equation. The material cost included in the objective function was set as a per-unit value (p.u/kg) relative to the unit cost per weight of each material constituting the motor. The total cost was then calculated by multiplying weights by unit cost per weight for each material calculated through LPM, where the unit cost per weight was set as iron to be 1, copper to be 6, and PM to be 60.

To minimize the possibilities of faults in the motor and high manufacturing cost, a concentrated winding armature and a PMa-SynRM rotor structure were adopted. Table 1 shows the design conditions of the down-scaled 3 kW PMa-SynRM proposed in this paper. Here, an optimal design was calculated based on minimum output torque of 16 Nm, efficiency of 95% at a base speed of 1800 r/min, and rated current of 10 Arms.

Table 1. Design specifications of a six-phase PMa-SynRM.

Design Specification		Desired Operating Specification	
Winding method	Concentrated	Rated currents [Arms]	10
Number of phases	6	Base torque [Nm]	16
Poles/slots	10/12	Base speed [r/min]	1800
Core material	35PN230	Max speed [r/min]	4500
Magnet material	N45H/1.4[T]	Rated Power [W]	3000
Line to line voltage [Vrms]	120	Min. efficiency [%]	95

3. Analysis of Results for Optimal Model

Optimal design results in Section 2 included stator and rotor-shape dimensions, phase resistance, no-load flux linkage, inductance, and efficiency. In particular, the shape data shown in Figure 6 immediately provided sketch data for FEM analysis, greatly reducing work time. In addition, the no-load flux linkage provided information on the magnitude of the magnetic torque according to Equation (1) and made it possible to infer the magnitude of the reluctance torque through the difference in inductance.

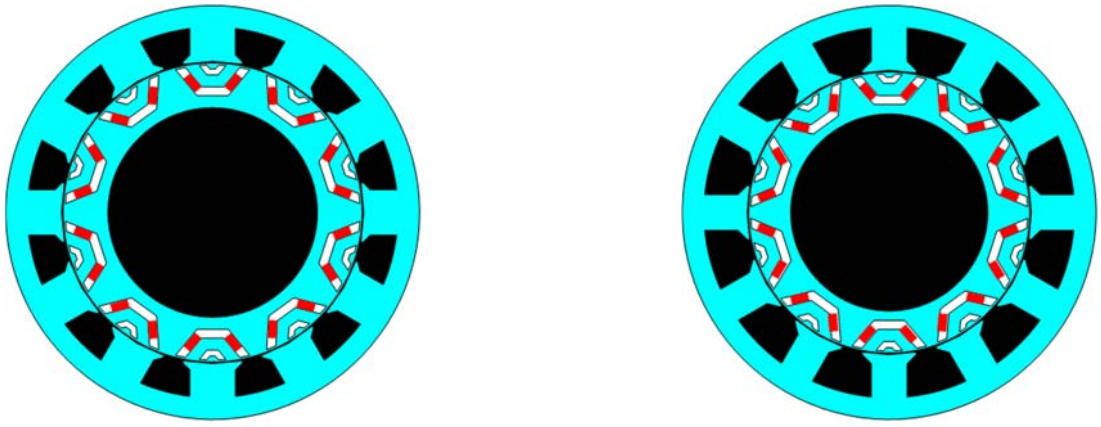

(**a**) (**b**)

Figure 6. Cross-section of designed six-phase PMa-SynRM. (**a**) Initial model before optimization; (**b**) Optimized model.

Figure 6a shows the shape of the initial model before optimization. Table 2 shows that the line to line voltage, power factor, and efficiency were analyzed to be 135.6 Vrms, 0.69, and 93.4% at base speed of 1800 r/min respectively. Figure 6b shows the optimized model, which was selected as a final candidate through the optimizing process, and whose line to line voltage, power factor, and efficiency were analyzed to be 120.0 Vrms, 0.848, and 95.3% at base speed of 1800 r/min respectively. In addition, Equation (21) confirmed that the cost was reduced. At the maximum speed of 4500 r/min, the torque decreased by 49% and 54% before and after optimization, respectively, and the power factor showed a tendency to increase. However, it was analyzed that RF increased to 12.1% before optimization and

decreased to 4.9% after optimization. In addition, the line to line voltage exceeded 120 Vrms in the initial model, but was less than 120 Vrms in the optimized model. In addition, it was found that the efficiency was higher after optimization.

Table 2. Results of designs before and after optimizing the process with LPM.

Parameters	Before Optimization		After Optimization	
Speed [r/min]	1800	4500	1800	4500
Rated current [Arms]	10	10	10	10
Line to Line voltage [Vrms]	135.6	128.9	120.0	116.8
Torque [Nm]	17.7	9.1	17.5	8.1
Ripple factor [%]	5.1	12.1	6.3	4.9
Power factor	0.690	1.0	0.848	0.960
Efficiency [%]	93.4	94.2	95.3	95.1
Material cost [p.u]	506.1	506.1	501.2	501.2

In this section, FEM analysis was performed using the design variable values derived through optimal LPM design. The test point for FEM analysis and the experiment was selected as 480 r/min, which is a speed causing minimal iron loss. For the constant-torque mode experiment performed in Section 5, 5 A was selected, which was one-half of the rated current.

3.1. Result of Optimal Design Specification

The results of the optimized LPM design under the conditions of Table 1 are presented in Table 2. The optimal design process, using LPM and the genetic algorithm, was carried out for a total of 250 generations with 50 individuals per generation. FEM analysis was performed at the optimal point, which is the maximal-efficiency point analyzed via LPM using the selected final model. In addition, FEM analysis was performed at the operating point in Table 1 to check whether the design requirements were satisfied. As a result, the efficiency at both analyzed points satisfied the requirement of $\geq$95%, and the analyzed torque at the design point was 17.2 Nm, which was larger than the reference torque of 16 Nm. The analytical result at the optimal point of LPM and the FEM analytical result were similar, thereby verifying the validity of the optimal design result. To compare with the experimental results, FEM analysis was also performed at the test point, and results are presented in Table 3.

Table 3. Result of analysis using LPM and FEM for a six-phase PMa-SynRM.

Parameters	LPM (Optimal Point)	FEM (Optimal Point)	FEM (Design Point)	FEM (Test Point)
Winding method	Concentrated	Concentrated	Concentrated	Concentrated
Number of series turns per phase	80	80	80	80
Resistance of phase [Ohm]	0.2087	0.2087	0.2087	0.2087
Base speed [r/min]	1800	1800	1800	480
Rated current [Arms]	5.0	5.0	10.0	5.0
Load angle [deg]	14.43	14.43	23	23
No-load linkage flux [Wbrms]	0.0512	0.0516	0.0516	0.0516
Output torque [Nm]	8.0	8.1	17.5	7.9
Copper loss [W]	31.2	31.2	124.7	31.2
Iron loss [W]	24.9	22.5	39.1	4.1
Efficiency [%]	96.3	96.6	95.3	91.8

3.2. BEMF Analysis

The back electromotive force (BEMF) is voltage induced when the magnetic flux generated in the permanent magnet is linked to the coil of the stator when the motor rotates under no-load conditions, and can be expressed as the product of the flux linkage and the

electric angular velocity, as shown in Equation (22). Therefore, magnetic torque, which is the first term in Equation (1), can be calculated with constant calculated flux linkage. In addition, since the BEMF is proportional to the speed, the ratio of the harmonic components analyzed through FFT did not change, and the relative torque pulsation level could be estimated through the size of the harmonic components. Figure 7a is a BEMF waveform analyzed at 480 r/min, and Table 4 shows the magnitude of the harmonic components of the phase voltage and the line voltage. The magnitude of the eleventh and thirteenth harmonic components affecting the torque pulsation during six-phase operation were analyzed to be 4.0% and 2.9% of the magnitude of the fundamental, respectively, and the magnitude of the fifth and seventh harmonic components affecting the three-phase operation were analyzed to be 7.0% and 3.1%, respectively.

$$E = \omega_e \lambda_{PM} \tag{22}$$

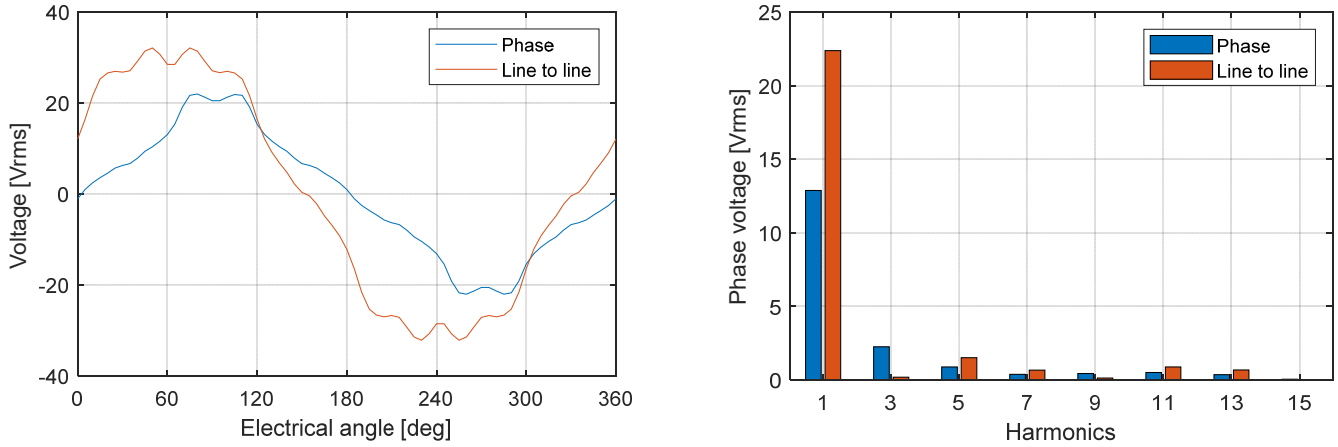

(**a**) (**b**)

Figure 7. BEMF calculation at 480 r/min using FEM. (**a**) Voltage curves; (**b**) FFT analysis.

Table 4. BEMF values by harmonics.

Harmonics	Phase Voltage [Vrms]	Line to Line Voltage [Vrms]
1	12.9	22.4
5	0.9	1.5
7	0.4	0.7
11	0.5	0.9
13	0.4	0.7

3.3. Inductance Analysis

D- and Q-axis inductance are important design factors that affect the magnitude of torque and voltage. As output torque in Equation (1) shows, the difference between the two inductances determines the reluctance torque magnitude, indicating that the optimized motor-shape design has a close relationship with output torque. Inductance was calculated using FEM analysis at 1800 r/min and 1 to 10 Arms, the same as the optimal LPM design condition, and the results are shown in Figure 8. The horizontal axis of the graph indicates the magnitude of D- and Q-axis currents, and the vertical axis indicates the inductance magnitude for each current. Inductance distribution shows that the Q-axis inductance appeared to be almost constant after 3A, while D-axis inductance, calculated through nonlinear analysis, had a relatively large difference in magnitude between LPM and FEM. Both Ld and Lq showed the largest error in the low-current section of 1–3 A, and the magnitude of error gradually increased after 6 A in Lq. The error in nonlinear D-axis inductance calculated at 10 A current was 0.5 mH, showing an error rate of approximately

8%, but there was no significant difference in the overall inductance distribution trend except for in the low-current section. Table 5 shows the maximum inductance values analyzed in LPM and FEM.

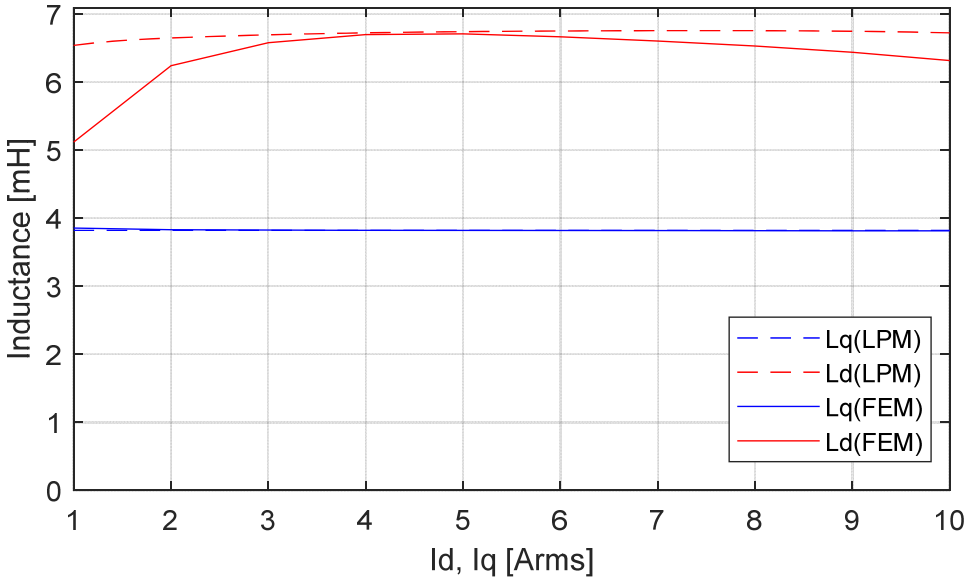

Figure 8. Comparison of inductance curves according to currents using LPM and FEM.

Table 5. Comparison of maximum inductance using LPM and FEM.

Parameter	L_q (LPM)	L_q (FEM)	L_d (LPM)	L_d (FEM)
Max. value [mH]	3.82	3.86	6.75	6.71

3.4. Torque Characteristics of Six- and Three-Phase Winding

It is possible to switch to three-phase motors with a six-phase asymmetric winding structure [29]. As shown in Figure 1, in the case of a six-phase asymmetric winding motor in which two three-phase windings are arranged with phases shifted 30 degrees from each other, if a fault occurs in one phase of the inverter or motor, it becomes a three-phase motor in the case of both of the other connected phases being opened. Figure 9 shows the torque curve for one cycle for six- and three-phase operation when the rated current was 10 A, analyzed using FEM. During six-phase operation, the average, maximal, and minimal torque values were interpreted to be 17.5, 18.1, and 17.0 Nm, respectively, and the ripple factor (RF) was calculated to be 6.3%. During three-phase operation, the average, maximal, and minimal torque values were interpreted to be 8.2, 8.7, and 7.8 Nm, respectively, and RF was calculated to be 11%. Therefore, the average torque during three-phase use decreased to 47% of the average output torque when all six phases were used, and the RF increased from 6.3% to 11%.

Additionally, load analysis was performed at a speed of 480 r/min to investigate the torque characteristics with respect to current. Since torque analysis through forced current injection is not affected by speed, it was analyzed by only increasing the current from 2 to 10 A. The analytical results are presented in Table 6 and show that as the current increased, the difference between output torque and maximal or minimal torque increased as well, and the RF showed a tendency to decrease.

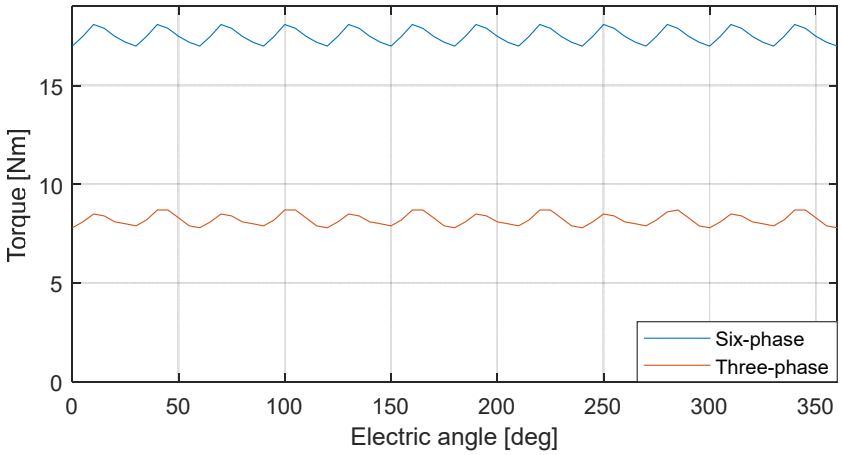

Figure 9. Torque curves of six and three phases from FEM analysis at 480 r/min and 10 A.

Table 6. Torque characteristic according to currents in FEM at 480 r/min.

Parameters		2 A	4 A	5 A	6 A	8 A	10 A
Six-phase	Max. torque [Nm]	3.4	6.8	8.5	10.4	14.2	18.1
	Min. torque [Nm]	2.9	6.1	7.7	9.5	13.1	17.0
	Mean torque [Nm]	3.1	6.4	8.1	9.9	13.6	17.5
	Difference of min/max [Nm]	0.5	0.7	0.8	0.9	1.1	1.1
	Ripple factor [%]	16.1	10.9	9.9	9.1	8.1	6.3
	Power factor	0.992	0.965	0.951	0.934	0.903	0.869
	Efficiency [%]	95.0	95.9	92.0	90.9	88.9	87.0
Three-phase	Max. torque [Nm]	1.8	3.5	4.3	5.2	6.9	8.7
	Min. torque [Nm]	1.4	2.8	3.6	4.4	6.1	7.8
	Mean torque [Nm]	1.6	3.2	4.0	4.8	6.5	8.2
	Difference of min/max [Nm]	0.4	0.7	0.7	0.8	0.8	0.9
	Ripple factor [%]	25.0	21.9	17.5	16.7	12.3	11.0
	Power factor	0.997	0.983	0.974	0.963	0.969	0.924
	Efficiency [%]	90.7	87.0	84.9	82.8	79.2	75.9

In Table 6, most RF values were large, which is analyzed as the effect of concentrated winding. In general, the air-gap flux density distribution is a square or trapezoidal waveform in the concentrated winding, which has large spatial harmonics, causing a large torque ripple. To reduce torque ripple, optimization methods of rotor and stator shapes have been proposed [32,33], but in this study, the optimization of design parameters to reduce the torque ripple of FSCW (fractional slot concentrated winding) was not considered.

For reference, the RF was calculated to be large at 2 A because the average torque was small, and therefore the difference between minimal and maximal torque was relatively large. However, the magnitude of its difference was the smallest.

3.5. Fault-Tolerant Operation Modes

Torque characteristics were analyzed for two fault states using FEM. The analysis was performed at 480 r/min with the UVW2 phase opened, as shown in Figure 1. The first was constant-current (CC) mode; since the magnitude of the phase current did not change, it was a control mode in which the output torque decreased when switching from six to three phases. The second was constant-torque (CT) mode, which was a control mode that maintained the output torque by doubling the phase current when switching from six to three phases. Therefore, 5 A, which is half the rated current of 10 A, was selected for the load current when switching to three-phase winding in the constant-torque mode, and the simulation was also conducted under 4 A to confirm the variation in torque ripple. In constant-torque mode, there is a risk of exceeding the rated current of the system, and therefore appropriate control scenarios and safeguards must be built in. Table 7 shows an

example of the operation of a six-phase motor that can be converted into a three-phases motor within a rated phase current of 10 A, and analysis was performed assuming that a phase current of 5 A flowed through the six-phase motor.

Table 7. Performance of each case of operation modes for six- and three-phase.

Parameters	6PH_5A	3PH_5A	3PH_10A	6PH_4A	3PH_4A	3PH_8A
Operation mode	Initial	CC	CT	Initial	CC	CT
Max. torque [Nm]	8.5	4.3	8.7	6.8	3.5	6.9
Min. torque [Nm]	7.7	3.6	7.8	6.1	2.8	6.1
Mean torque [Nm]	8.1	4.0	8.2	6.4	3.2	6.5
Difference of min/max [Nm]	0.8	0.7	0.9	0.7	0.7	0.8
Ripple factor [%]	9.9	17.5	11.0	10.9	21.9	12.3
Power factor	0.951	0.974	0.924	0.965	0.983	0.969
Efficiency [%]	92.0	84.9	75.9	95.9	87.0	79.2

Here, when comparing the average torque of 6PH_5A and 3PH_10A, which generated MMF of the same magnitude, differences as large as 0.1 Nm were found in the three-phase condition, but this value is within the analytical margin of error. When comparing RF, the RF in the three-phase condition was interpreted as a 1.1% larger value, which represents a significant increase. This increase in torque ripple appears to be influenced by the 5th and 7th harmonics analyzed through Figure 7b during three-phase operation.

If the constant-current mode was applied at 6PH_5A, the state was converted into 3PH_5A, and the average torque was reduced to 49% of the original level. In this case, since the torque was small, it could only be applied in a light-load situation. However, if the constant-torque mode was applied within a limit that did not exceed the rated current range, operation with 3PH_10A became possible, and an average torque similar to that of 6PH_5A operation could be obtained. The conditions for this situation to be possible are either when the system is operated with a load less than half the maximal allowable phase current in the system or when the maximal current of the system is forcibly limited within the rated current. Therefore, if phase-switching and current-control functions could be implemented in a variety of ways through the study of the operation characteristics of a six-phase motor with a high degree of freedom, it could be possible to create strategic operation scenarios that both avoid faults and extend the lifespan of system components.

4. Experimental Results for 3 kW Six-Phase PMa-SynRM

The motor manufactured based on the optimal LPM design result is shown in Figure 10. For the motor-performance test, a 7.5 kW servo motor, three-phase inverter, DC input power supply, torque sensor, and DSP were used in the experimental system. Figure 11 shows the assembly of the experimental instrument. The torque sensor used in this study was of a type that could only measure the average torque 30 times per rotation of the rotor shaft. Therefore, information on torque ripple could not be provided through experimental results.

(**a**) (**b**)

Figure 10. Manufactured motor; (**a**) Stator, (**b**) rotor.

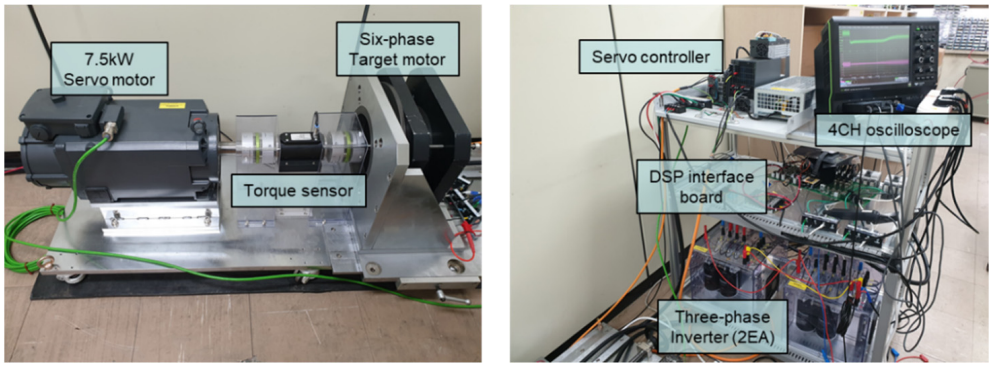

Figure 11. Experimental setup for testing.

The specifications of each instrument are presented in Table 8. Six- and three-phase BEMF and load tests in a steady state condition were conducted under the conditions of 480 r/min and 2–10 A, as shown in Table 6. Table 3 shows that low efficiency at the test point was meaningless, so it was excluded from analysis of the experimental results.

Table 8. The experimental instruments.

Instrument	Model
Servo motor	HD-805
Torque sensor	M425-S1 C
Oscilloscope	6510e
DC power supply	500 V 30 A (15 kW)
3ph Inverter ×2	Semikron AN-8005
DSP	F28379D
JTAG emulator	XDS100 ver3.0

The experiment proceeded as follows. First, the test speed was attained through speed control in the servo motor. At this time, the six-phase motor operated in generating mode, and when the load current was not applied, the back electromotive force could be measured. Here, when a load current was applied to the motor, it became a motoring mode, and torque was generated by a rotating force in the opposite direction.

4.1. BEMF Characteristic on No Load

The measured BEMF in the experiment was line-to-line voltage of 21.91 Vrms, which was approximately the same value as the FEM result from Table 4 (21.5 Vrms) with a difference of 0.4 Vrms. The voltage waveform in Figure 12 was the same as the BEMF waveform in Figure 7 determined through FEM. Therefore, the calculated no-load flux linkage had the same value in both FEM analysis and the experiment.

4.2. Torque Characteristic on Load

In order to confirm the torque characteristics in the steady state, a load test was performed for six-phase operation at 480 r/min. The average torque for each current was measured by setting the D- and Q-axis currents between 2 to 10 A, and the same load angle was applied as that in the FEM analysis results in Table 6. Average torque, error rate, torque constant, and torque RF for each current are shown in Table 9.

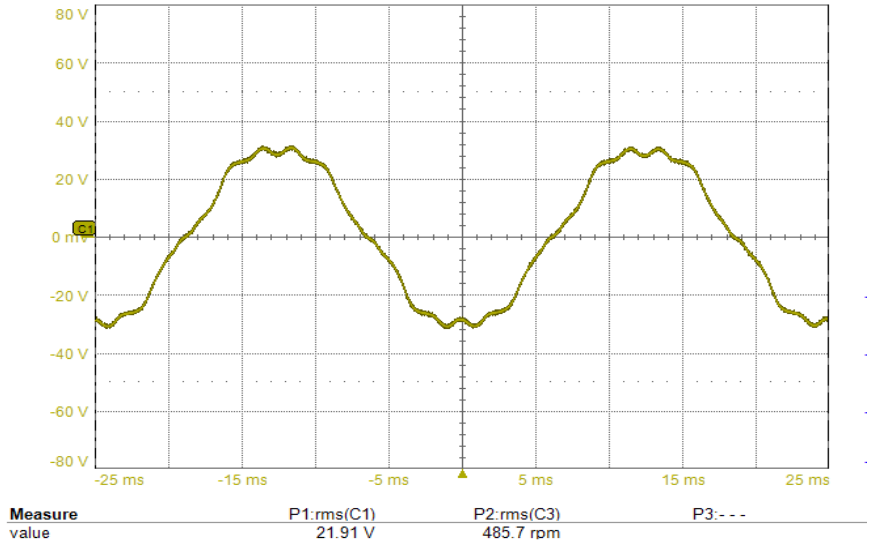

Figure 12. BEMF curve at 480 r/min.

Table 9. Comparison of torque characteristics in relation to current for six-phase operation.

Currents [Arms]	Load Angle [deg]	Torque FEA [Nm]	Torque Exp. [Nm]	Torque Error [%]	Torque Constant
2	6	3.1	2.9	6.9	1.45
4	12	6.4	6.1	4.9	1.53
5	15	8.1	7.7	5.2	1.54
6	17	9.9	9.3	6.5	1.55
8	21	13.6	12.9	5.4	1.61
10	23	17.5	16.4	6.7	1.64

The error rate of the average torque obtained through FEM analysis and experimental results was the largest at 6.9% at 2 Arms, but the magnitude of the difference in torque was 0.2 Nm, which was negligible. At the rated 10 A, the torque error rate was 6.7% and the magnitude was 1.1 Nm, which could also be considered to be within the error range. The torque constant, which denotes the average torque per current, increased from 1.45 to 1.64 Nm/Arms as the current increased, and the average torque constant was calculated to be 1.55 Nm/Arms.

As a result, the measured average torque satisfied the design requirements presented in Table 1, so the validity of the optimal design using LPM was verified through the experiment. Figure 13 shows the curves for the current and torque of a six-phase operation measured at a rated current of 10 A and a load angle of 23 deg, displaying U1 voltage, U1 current, torque, and speed at the upper-left corner.

Next, an experiment was performed with a three-phase winding assuming a fault state, as shown in Figure 1. The experiment was conducted under the same operating conditions as those of the six-phase one, and results are shown in Table 10 and Figure 14. The actual measured RF value was significantly reduced compared to the FEM analysis results in Table 6 for three-phase operation, as in the RF results measured during six-phase operation. The average torque during three-phase operation was between 47% and 48% of that of six-phase operation, and the torque ratio showed a decreasing trend as the current increased. This phenomenon occurred because the magnetic flux that should have been concentrated in the stator core of UVW1, which was operating normally, leaked into the core of the UVW2 phase that had a fault [34]. Figure 15 shows the magnetic flux density distribution of six- and three-phase FEM simulations, respectively; magnetic flux, which was low in Figure 15a, increased in the box region of Figure 15b, which was a fault condition. In addition, as the magnitude of the current increased, magnetic resistance increased due to the saturation of the stator iron core, resulting in an increase in the amount of leaked

magnetic flux. Therefore, when switching from six to three phases, the output torque could not exactly reach 50% due to magnetic flux leakage.

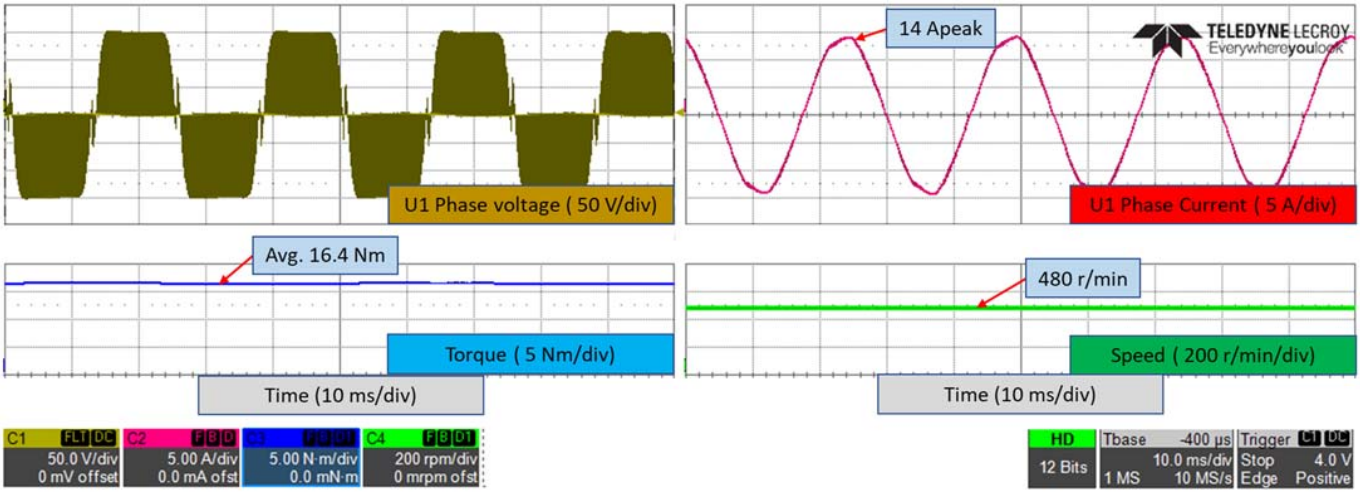

Figure 13. Torque curves at 480 r/min and 10 A for six-phase operation.

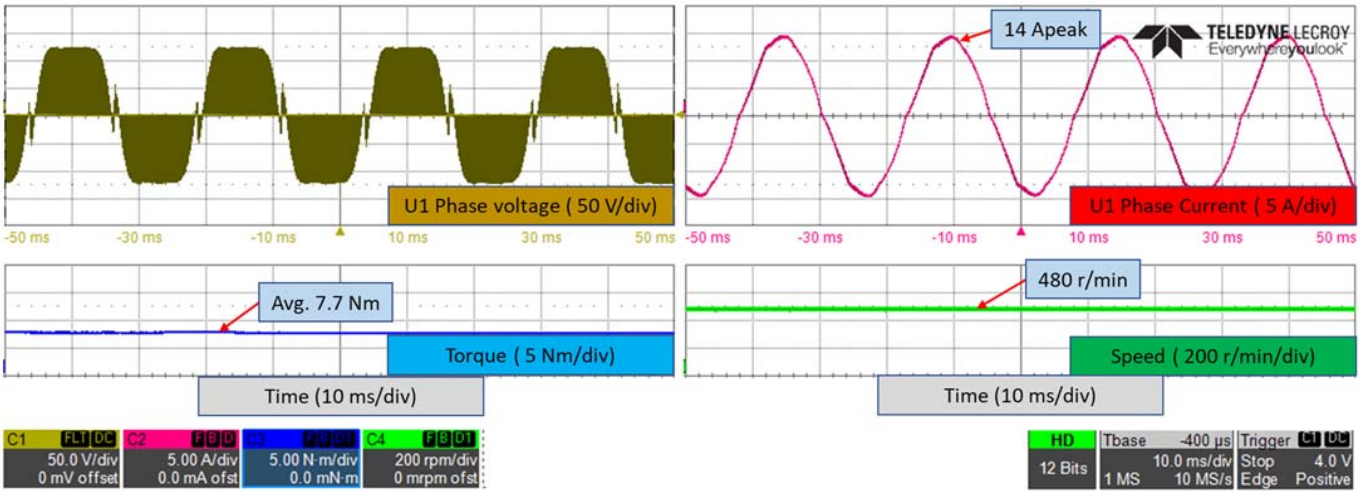

Figure 14. Torque curves at 480 r/min and 10 A for three-phase operation.

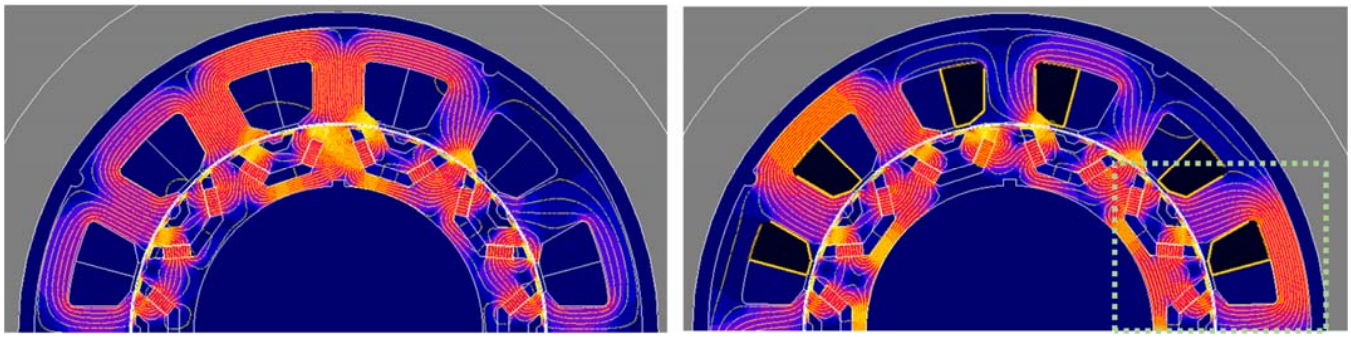

(**a**) (**b**)

Figure 15. Flux density plot of (**a**) six- and (**b**) three-phase operation.

Table 10. Comparison of torque characteristics in relation to current for three-phase operation.

Currents [Arms]	Load Angle [deg]	Torque FEA [Nm]	Torque Exp. [Nm]	Torque Error [%]	Torque Constant
2	6	1.6	1.4	14.3	0.70
4	12	3.2	3.0	6.7	0.75
5	15	4.0	3.8	6.7	0.75
6	17	4.8	4.5	6.7	0.75
8	21	6.5	6.1	6.6	0.76
10	23	8.2	7.7	6.5	0.77

5. Transient-State Analysis for Switching from Six- to Three-Phase Operation

In Section 4, the load characteristics in the steady state were analyzed in detail. Subsequently, it was necessary to investigate changes in voltage, current, and torque when switching from six- to three-phase operation. Here, the data obtained through transient analysis during phase switching could be used as a reference when designing the controller and inverter of the fault-tolerant system. The phase switching experiment was conducted by changing the control program for each mode.

To switch from six- to three-phase operation as shown in Figure 16, the input and output of INV2 must be limited to zero in the controller. Here, the output variable of SVPWM, which is the input of the inverter, was set to zero, and the three-phase switch of INV2 was turned off using the trip function to prevent malfunction. At this time, according to the state of the Clarke transformation matrix of the fed-back current, operation could be divided into constant-current and constant-torque modes. In a normal six-phase operation, a six-phase Clarke transformation matrix is applied and multiplied by a scaling factor of 1/3, as shown in Equation (23). However, when converting from six to three phases, a three-phase Clarke transformation matrix must be applied as shown in Figure 16. Here, constant-current mode was controlled through Equation (24) to keep the phase current constant, and the torque was reduced by half. On the other hand, constant-torque mode was controlled to keep the MMF generated in the stator in its original state through Equation (25); subsequently, phase current was doubled.

$$T_c = \frac{1}{3}\begin{bmatrix} 1 & cos(\theta) & cos(4\theta) & cos(5\theta) & cos(8\theta) & cos(9\theta) \\ 0 & sin(\theta) & sin(4\theta) & sin(5\theta) & sin(8\theta) & sin(9\theta) \\ 1 & cos(5\theta) & cos(8\theta) & cos(\theta) & cos(4\theta) & cos(9\theta) \\ 0 & sin(5\theta) & sin(8\theta) & sin(\theta) & sin(4\theta) & sin(9\theta) \\ 1 & 0 & 1 & 0 & 1 & 0 \\ 0 & 1 & 0 & 1 & 0 & 1 \end{bmatrix} \tag{23}$$

$$T_c = \frac{2}{3}\begin{bmatrix} 1 & cos(4\theta) & cos(8\theta) \\ 0 & sin(4\theta) & sin(8\theta) \\ 0 & 0 & 0 \end{bmatrix} \tag{24}$$

$$T_t = \frac{1}{3}\begin{bmatrix} 1 & cos(4\theta) & cos(8\theta) \\ 0 & sin(4\theta) & sin(8\theta) \\ 0 & 0 & 0 \end{bmatrix} \tag{25}$$

First, a phase-switching experiment was conducted to stop UVW2, using Equation (24) at 480 r/min and 5 A, to obtain transient-state curves of UVW1 for constant-current mode. The result is shown in Figure 17, and changes were observed in current and torque, excluding voltage. Figure 17 shows the U1-V1 voltage, U1 current, U2 current, and torque in that order. At the beginning of the transient state of the constant-current mode, the peak current of U1 increased from 7 to 15 A, and the steady state was restored after approximately 85 ms. However, the torque did not immediately respond to the current change and started to change from 7.7 to 8.6 Nm after approximately 12 ms after the time

of phase change, and then decreased to half of the initial torque after 55 ms. The contents described above were shown in Table 11.

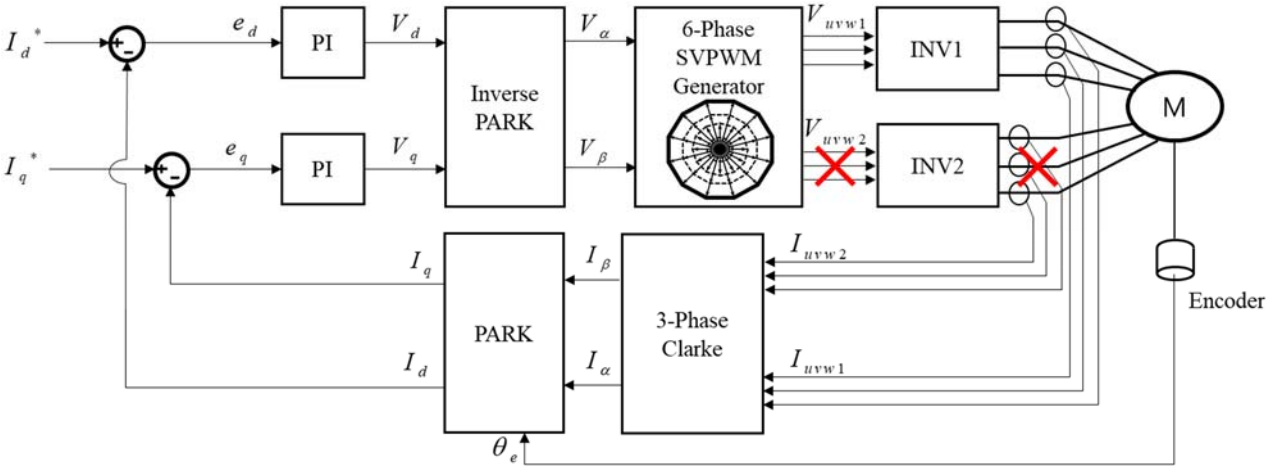

Figure 16. Block diagram for switching control from six- to three-phase operation.

Table 11. Transient state of constant-current mode.

Modes	Peak Current [A]	Max. Torque [Nm]	Transient Time [ms]
Initial state	7	7.7	-
Constant current	15	8.6	85

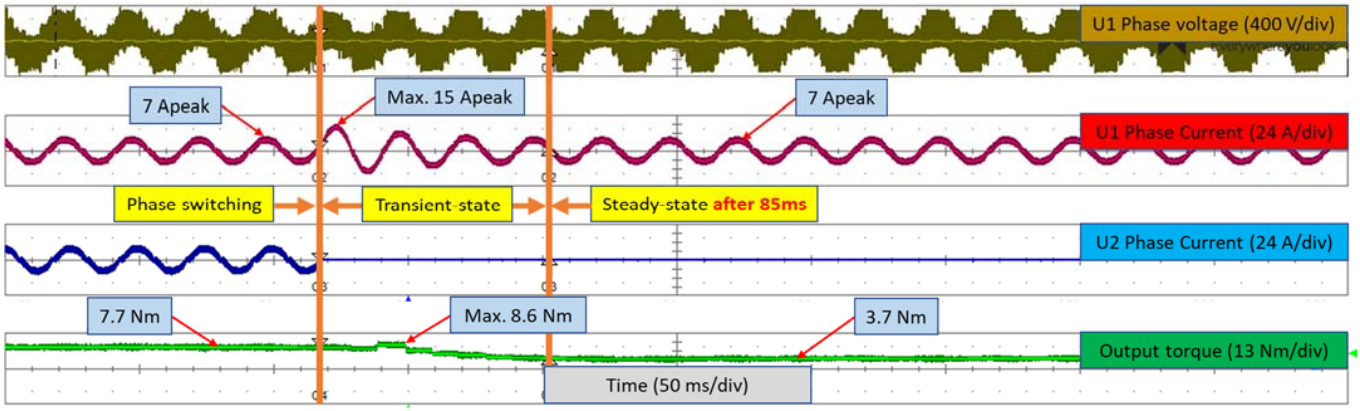

Figure 17. Transient state of constant-current mode at 480 r/min and 5 A.

After that, in order to obtain transient state curves for the constant-torque mode, Equation (25) was used at 480 r/min and 5 A to conduct an experiment. The result is shown in Figure 18. As in constant-current mode, peak current increased by approximately 2.8 times from 7 to 20 A, and then gradually decreased for 135 ms, maintaining a steady state at twice the original current. The torque increased from approximately 7.7 to 11.2 Nm as the current momentarily increased, and then returned to the initial level. However, as in the constant-current mode, torque change started after approximately a 13 ms delay from the time of phase change. The contents described above were shown in Table 12.

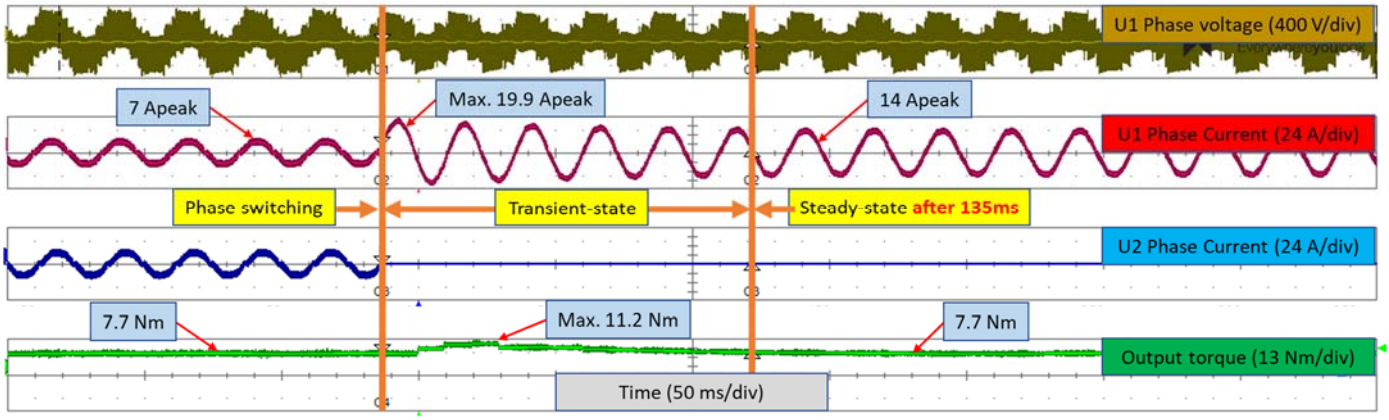

Figure 18. Transient state of constant-torque mode at 480 r/min and 5A.

Table 12. Transient state of constant-torque mode.

Modes	Peak Current [A]	Max. Torque [Nm]	Transient Time [ms]
Initial state	7	7.7	-
Constant torque	19.9	11.2	135

The transient times for constant-current and constant-torque modes presented above were 85 and 135 ms, respectively, and the time difference between the modes from transient to steady-state during phase change was therefore 50 ms. Transient time is summarized in Table 13 by dividing it into current and torque for each mode. Here, U2 current was not included because it was immediately cut off during phase change.

Table 13. Comparison of detailed transient-state time.

Modes		Control Point [ms]	Changing Point [ms]	End Point [ms]	Total Time [ms]
Constant current	U1 Current	−32	−32	53	85
	Torque	−32	−20	53	85
Constant torque	U1 Current	−13	−13	122	135
	Torque	−13	0	122	135

6. Conclusions

In this paper, the design process of a 3 kW down-scaled six-phase PMa-SynRM that is capable of three-phase switching was explained on the basis of magnetic circuit theory, and results were presented. The validity of the design was verified by performing FEM simulation analysis on the basis of optimal-design LPM data. FEM analysis results were verified by performing load experiments for six- and three-phase operations between 2 and 10 A. As a result, output torque error was less than 7%, except for the low current of 2 A during six-phase operation. Here, it can be seen that the analyzed torque value appeared slightly larger when considering that the actual experimental result and the torque presented within design conditions were similar; this can be improved by adjusting some variables in the LPM optimal design.

In addition, the feasibility of the three-phase fault operation capability of the six-phase motor presented in [30] was verified through experiments. Current- and torque-constant control modes implemented through phase switching were analyzed on the basis of phase current and torque curves. As a result, in the transient state, the current and torque curves of U1 showed a transient state, but U1 voltage did not show any significant change, and U2 current was cut off when control started. In the case of torque, as a result of repeated experiments, both current- and torque-constant modes showed a transient state with a time delay of approximately 12 to 13 ms. The duration of the total transient state was 85 ms in

constant-current control mode, and 135 ms in constant torque control mode, which showed that steady-state operation was restored within a short time.

Phase-switching technology utilizing the six-phase motor's multiple degrees of freedom could be applied both to the ability to respond to fault condition on the system, and to an efficient energy-management strategy tailored to the driving environment of EVs. In addition, if the technology for switching from a six- to a three-phase system was expanded to four- or five-phase systems, a multiple-degrees-of-freedom system with higher output torque and lower torque ripple than those of a three-phase system can be realized. Therefore, as an alternative to overcome the limitations of existing three-phase EV systems, we propose a six-phase motor that can be configured as a multiple-degrees-of-freedom system for fault tolerance.

Author Contributions: Design and application—D.H.; Literature review, manuscript preparation and simulations—D.H., D.Y.; Experimental verification—D.H., D.Y. and J.B.; Final review of manuscript, corrections—J.B. All authors have read and agreed to the published version of the manuscript.

Funding: This research was funded by grant (2018R1D1A3B0704376414) from National Research Foundation of Korea (NRF), a research grant from Hyundai Motor Group and supported by grant (P0008458, The Competency Development Program for Industry Specialist) from Korea Institute for Advancement of Technology (KIAT) grant funded by the Korea Government (MOTIE).

Institutional Review Board Statement: Not applicable.

Informed Consent Statement: Not applicable.

Data Availability Statement: Not applicable.

Conflicts of Interest: The authors declare no conflict of interest.

References

1. Guan, Y.; Zhu, Z.Q.; Afinowi, I.A.A.; Mipo, J.C.; Farah, P. Comparison between induction machine and interior permanent magnet machine for electric vehicle application. In Proceedings of the 2014 17th International Conference on Electrical Machines and Systems (ICEMS), Hangzhou, China, 22–25 October 2014; pp. 144–150.
2. Toliyat, H.A.; Lipo, T.A.; White, J.C. Analysis of a concentrated winding induction machine for adjustable speed drive applications—Part II: Motor design and performance. *IEEE Trans. Energy Convers.* **1991**, *6*, 684–692. [CrossRef]
3. Lyra, R.; Lipo, T.A. Torque density improvement in a six-phase induction motor with third harmonic current injection. *IEEE Trans. Ind. Appl.* **2002**, *38*, 1351–1360. [CrossRef]
4. Xu, H.; Toliyat, H.A.; Petersen, L.J. Rotor field oriented control of five-phase induction motor with the combined fundamental and third harmonic currents. *Proc. IEEE APEC* **2001**, *1*, 392–398.
5. Xu, H.; Toliyat, H.A.; Petersen, L.J. Five-phase induction motor drives with DSP-based control system. *IEEE Trans. Power Electron.* **2002**, *17*, 524–533. [CrossRef]
6. Sala, G.; Mengoni, M.; Rizzoli, G.; Zarri, L.; Tani, A. Decoupled d–q Axes Current-Sharing Control of Multi-Three-Phase Induction Machines. *IEEE Trans. Ind. Electron.* **2020**, *67*, 7124–7134. [CrossRef]
7. Benatmane, M.; McCoy, T.; Dalton, T.; Cooper, T.L. Electric power generation and propulsion motor development for US Navy surface ships. In Proceedings of the All Electric Ship: Developing Benefits Maritime Application Conference, London, UK, 1 September 1998; pp. 89–94.
8. Norton, P.T.; Thompson, P.E. The naval electric ship of today and tomorrow. In Proceedings of the 3rd All Electric Ship Symposium, Paris, France, 26–27 October 2000; pp. 80–86.
9. Mantero, S.; Monti, A.; Spreafico, S. DC-bus voltage control for double star asynchronous fed drive under fault conditions. In Proceedings of the 2000 IEEE 31st Annual Power Electronics Specialists Conference. Conference Proceedings (Cat. No. 00CH37018), Galway, Ireland, 23 June 2000; pp. 533–538.
10. Dutta, R.; Rahman, M.F. Design and Analysis of an Interior Permanent Magnet (IPM) Machine With Very Wide Constant Power Operation Range. *IEEE Trans. Energy Convers.* **2008**, *23*, 25–33. [CrossRef]
11. Cao, R.; Mi, C.; Cheng, M. Quantitative Comparison of Flux-Switching Permanent-Magnet Motors With Interior Permanent Magnet Motor for EV, HEV, and PHEV Applications. *IEEE Trans. Magn.* **2012**, *48*, 2374–2384. [CrossRef]
12. Xue, P.; Lin, J. Discussion on the Rare earth resources and its development potential of Inner Mongolia of China. In Proceedings of the 2011 International Conference on Materials for Renewable Energy & Environment, Shanghai, China, 20–22 May 2011; Volume 1, pp. 9–12.

13. Boldea, I.; Tutelea, L.; Pitic, C. PM-Assisted Reluctance Synchronous Motor/Generator (PM-RSM) for Mild Hybrid Vehicles: Electromagnetic Design. *IEEE Trans. Ind. Appl.* **2004**, *40*, 492–498. [CrossRef]
14. Barcaro, M.; Bianchi, N.; Magnussen, F. Design considerations to maximize performance of an IPM motor for a wide flux-weakening region. In Proceedings of the XIX International Conference on Electrical Machines—ICEM 2010, Rome, Italy, 6–8 September 2010; pp. 1–7.
15. Guglielmi, P.; Boazzo, B.; Armando, E.; Pellegrino, G.; Vagati, A. Permanent-Magnet Minimization in PM-Assisted Synchronous Reluctance Motors for Wide Speed Range. *IEEE Trans. Ind. Appl.* **2013**, *49*, 31–41. [CrossRef]
16. Wang, B.; Wang, J.; Sen, B.; Griffo, A.; Sun, Z.; Chong, E. A Fault-Tolerant Machine Drive Based on Permanent Magnet-Assisted Synchronous Reluctance Machine. *IEEE Trans. Ind. Appl.* **2018**, *54*, 1349–1359. [CrossRef]
17. Fu, J.R.; Lipo, T.A. Disturbance-free operation of a multiphase current-regulated motor drive with an opened phase. *IEEE Trans. Ind. Appl.* **1994**, *30*, 1267–1274.
18. Toliyat, H.A. Analysis and simulation of five-phase variable-speed induction motor drives under asymmetrical connections. *IEEE Trans. Power Electron.* **1998**, *13*, 748–756. [CrossRef]
19. Xu, H.; Toliyat, H.A.; Petersen, L.J. Resilient current control of five-phase induction motor under asymmetrical fault conditions. In Proceedings of the APEC—Seventeenth Annual IEEE Applied Power Electronics Conference and Exposition (Cat. No. 02CH37335), Dallas, TX, USA, 10–14 March 2002; Volume 1, pp. 64–71.
20. Wang, K.; Gu, Z.; Liu, C.; Zhu, Z.Q. Design and Analysis of a Five-Phase SPM Machine Considering Third Harmonic Current Injection. *IEEE Trans. Energy Convers.* **2018**, *33*, 1108–1117. [CrossRef]
21. Baek, J.; Bonthu, S.S.R.; Choi, S. Design of five-phase permanent magnet assisted synchronous reluctance motor for low output torque ripple applications. *IET Electr. Power Appl.* **2016**, *10*, 339–346. [CrossRef]
22. Sui, Y.; Zheng, P.; Yin, Z.; Wang, M.; Wang, C. Open-Circuit Fault-Tolerant Control of Five-Phase PM Machine Based on Reconfiguring Maximum Round Magnetomotive Force. *IEEE Trans. Ind. Electron.* **2019**, *66*, 48–59. [CrossRef]
23. Zhao, Y.; Lipo, T. Space vector PWM control of dual three-phase induction machine using vector space decomposition. *IEEE Trans. Ind. Appl.* **1995**, *31*, 1100–1109. [CrossRef]
24. Barcaro, M.; Bianchi, N.; Magnussen, F. Six-phase supply feasibility using a PM fractional-slot dual winding machine. In Proceedings of the 2010 IEEE Energy Conversion Congress and Exposition, Atlanta, GA, USA, 12–16 September 2010; pp. 1058–1065. [CrossRef]
25. Bonthu, S.S.R.; Choi, S.; Baek, J. Design Optimization With Multiphysics Analysis on External Rotor Permanent Mag-net-Assisted Synchronous Reluctance Motors. *IEEE Trans. Energy Convers.* **2018**, *33*, 290–298. [CrossRef]
26. Hashemnia, N.; Asaei, B. Comparative study of using different electric motors in the electric vehicles. In Proceedings of the 2008 18th International Conference on Electrical Machines, Vilamoura, Portugal, 6–9 September 2008; pp. 1–5.
27. Deng, X.; Mecrow, B.; Wu, H.; Martin, R. Design and Development of Low Torque Ripple Variable-Speed Drive System With Six-Phase Switched Reluctance Motors. *IEEE Trans. Energy Convers.* **2018**, *33*, 420–429. [CrossRef]
28. Jeong, H.; Lee, H.; Kwak, S.; Kim, N.; Baek, J. Analysis of IPMSM Characteristics in Conversion of Six to Three-Phase for Fault Tolerant Operation. In Proceedings of the 2019 IEEE R10 Humanitarian Technology Conference (R10-HTC)(47129), Depok, Indonesia, 12–14 November 2019; pp. 149–152.
29. Feng, G.; Lai, C.; Li, W.; Tjong, J.; Kar, N.C. Open-Phase Fault Modeling and Optimized Fault-Tolerant Control of Dual Three-Phase Permanent Magnet Synchronous Machines. *IEEE Trans. Power Electron.* **2019**, *34*, 11116–11127. [CrossRef]
30. Catuogno, G.R.; García, G.; Leidhold, R. Fault tolerant control in six-phase PMSM under four open-circuits fault conditions. In Proceedings of the IECON 2016—42nd Annual Conference of the IEEE Industrial Electronics Society, Florence, Italy, 23–26 October 2016; pp. 5754–5759.
31. Hu, Y.; Zhu, Z.Q.; Odavic, M. Torque Capability Enhancement of Dual Three-Phase PMSM Drive With Fifth and Seventh Current Harmonics Injection. *IEEE Trans. Ind. Appl.* **2017**, *53*, 4526–4535. [CrossRef]
32. Park, J.; Kim, S.; Hong, J.; Lee, J. Rotor Design on Torque Ripple Reduction for a Synchronous Reluctance Motor With Concentrated Winding Using Response Surface Methodology. *IEEE Trans. Magn.* **2006**, *42*, 3479–3481. [CrossRef]
33. Choi, Y.-C.; Lee, J.-H. Rotor & Stator Design on Torque Ripple Reduction for a Synchronous Reluctance Motor with a Concentrated Winding using RSM. In Proceedings of the 2007 International Conference on Electrical Machines and Systems (ICEMS), Seoul, Korea, 8–11 October 2007; pp. 1216–1221.
34. Babetto, C.; Bianchi, N. Synchronous Reluctance Motor with Dual Three-Phase Winding for Fault-Tolerant Applications. In Proceedings of the 2018 XIII International Conference on Electrical Machines (ICEM), Alexandroupoli, Greece, 3–6 September 2018; pp. 2297–2303.